Investigation of Frequency Effects on the Performance of Single-Sided Linear Induction Motor

Abbas Shiri and Abbas Shoulaie

Department of Electrical Engineering
Iran University of Science and Technology, Tehran, Iran
abbas_shiri@iust.ac.ir, Shoulaie@iust.ac.ir

Abstract ─ Single-sided linear induction motors (SLIMs) have been widely used in industry, especially in high-speed transportation systems. The performance of the SLIMs is considerably affected by the characteristics of its secondary back-iron. The conductivity of the iron used as well as its magnetic permeability influence the performance of the machine, while the magnetic permeability itself is affected by the input frequency of the SLIM. In this paper, using Dancan equivalent circuit model and considering all phenomena involved in the single-sided linear induction motor, the outputs of the motor such as efficiency, power factor, normal force and output thrust are analytically derived. Then, the effects of the input frequency on depth of the field penetration and saturation level of the secondary back-iron as well as the SLIM outputs are analyzed. To confirm the analytical results, 2D time-stepping finite element method is employed. The results are in good agreement with each other confirming the analytical analysis.

Index Terms ─ Back-iron saturation, efficiency, input frequency, normal force, output thrust, power factor.

I. INTRODUCTION

Single-sided linear induction motor (SLIM) is one of the many kinds of linear motors that became popular in industry in recent decades. Their simple structure and comparatively low construction cost make them a reliable candidate for high-speed transportation systems [1, 2]. Because of the importance of the SLIM, it has gained interests of the researchers in industry. Many investigations have been done concerning the design of the SLIMs. In design, the primary weight [3], the thrust and power to weight ratio [4], the power factor and efficiency [5-7], and thrust in constant current [8] have been considered. To study the performance of the SLIMs, several equivalent circuit models have been proposed which facilitate their analysis [9-11]. There are special phenomena in linear motors that make them different from their rotary counterparts. Lee et al. have investigated the effect of the construction of the secondary on edge effect [12]. There are some researches which investigate the end effect in linear induction motors. Bazghaleh et al. have designed the SLIM considering end effect phenomenon [13-15]. In [16], the existence of the end effect has been confirmed by using analytical equations and defining end effect factor. Also, the effects of design parameters on the end effect have been investigated in [17-19].

In double-layer secondary SLIM, the performance of the latter is mainly influenced by saturation level of the back-iron. The secondary back-iron plays important role in operation of the SLIM. Besides providing a mechanical support, it is used as magnetic flux pass produced by the primary. Changing the input frequency changes the saturation level of the back-iron and so, impresses the performance of the motor. In this paper, to study the performance of the SLIM, analytical equations for the efficiency, power factor, normal force and output thrust are derived. All phenomena involved in the single-sided linear induction motor such as longitudinal end effect, back-iron saturation, transverse edge effect, and skin effect are considered in equations. Then, using the derived equations, the frequency effects

Submitted On: Jan. 12, 2012
Accepted On: April 25, 2012

on the saturation level of the back-iron and the motor performance are investigated. To confirm the validity of the analytical analysis, as well as the obtained outputs, finite element method is employed and the results are compared.

II. EQUIVALENT CIRCUIT MODEL OF THE SLIM

Similar to rotary induction motors, the performance of SLIM can be investigated by equivalent circuit model [9-11]. For investigation of the performance of the SLIM, the equivalent circuit model proposed by Duncan is employed [9]. The per-phase equivalent circuit model is shown in Fig. 1. In this figure, R_1 is the per-phase resistance of the primary which is calculated as follows:

$$R_1 = \frac{2(W_s + l_{ec})N}{\sigma_w A_w}, \quad (1)$$

In the above equation, σ_w is the conductivity of the conductor used in the primary winding, l_{ec} is the end connection length, W_s primary width, N the per-phase number of turns of the primary winding and A_w is the cross-sectional area of the conductor.

The primary leakage reactance is given by [20, 21]:

$$X_1 = 2\mu_0\omega_1[(\lambda_s(1+\frac{3}{2p})+\lambda_d)\frac{W_s}{q}+\lambda_e l_{ec}]N^2/p, \quad (2)$$

where μ_0 is the permeability of the vacuum, p the number of pole pairs, q the number of the slots per pole per phase, ω_1 the primary angular frequency and λ_s, λ_e and λ_d are the permeances of slot, the end connection and the differential, respectively.

The per-phase magnetizing reactance of the motor is given by [20]:

$$X_m = \frac{6\mu_0\omega_1 W_{se} {k_w}^2 N^2 \tau}{\pi^2 p g_e}, \quad (3)$$

where k_w is the winding factor, τ the pole pitch and W_{se} and g_e are the equivalent primary width and the effective air-gap length, respectively, which are calculated by the following equations:

$$W_{se} = W_s + g_m, \quad (4)$$

$$g_e = (k_c k_l / k_{tm})(1+k_s)g_m, \quad (5)$$

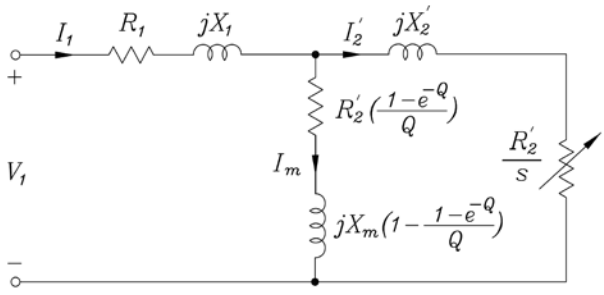

Fig. 1. Equivalent circuit of SLIM.

In the aforementioned equations, the following denotations and equations are hold:

g_m is the magnetic air-gap, k_l the air-gap leakage factor, k_c the Carter's coefficient, k_{tm} the magnetizing reactance factor due to edge effect, and k_s is the secondary iron saturation factor. The mentioned coefficients are given as follows:

$$g_m = g + d, \quad (6)$$

$$k_l = \frac{\sinh(\pi g_m/\tau)}{\pi g_m/\tau}, \quad (7)$$

$$k_c = \frac{\tau_s}{\tau_s - \gamma g_m}, \quad (8)$$

$$\gamma = (w_s/g_m)^2/[5+(w_s/g_m)], \quad (9)$$

$$k_{tm} = (k_R/k_x)k_{tr}, \quad (10)$$

$$k_{tr} = \frac{{k_x}^2}{k_R}\frac{1+(sGk_R/k_x)^2}{1+(sG)^2}, \quad (11)$$

$$k_R = 1 - \mathrm{Re}[(1-jsG)\frac{2\lambda}{\alpha W_{se}}\tanh(\frac{\alpha W_{se}}{2})], \quad (12)$$

$$k_x = 1 + \mathrm{Re}[(sG+j)\frac{2sG\lambda}{\alpha W_{se}}\tanh(\frac{\alpha W_{se}}{2})], \quad (13)$$

$$\lambda = \frac{1}{1+\sqrt{1+jsG}\tanh(\frac{\alpha W_{se}}{2})\tanh[\pi(c-\frac{W_{se}}{2})/\tau]}, \quad (14)$$

$$\alpha = (\pi/\tau)\sqrt{1+jsG}, \quad (15)$$

$$G = \frac{2\mu_0 f_1 \tau^2 \sigma_e d}{\pi g_m k_l k_c (1+k_s)}, \quad (16)$$

$$k_s = \mu_0(\tau/\pi)^2(\mu_i\delta_i g_m k_c)^{-1}, \quad (17)$$

$$\delta_i = \mathrm{Re}[\frac{1}{\sqrt{(\pi/\tau)^2 + j2\pi f_1 \mu_i s\sigma_i/k_{tri}}}], \quad (18)$$

$$k_{tri} = [1-(\frac{2\tau}{\pi W_{se}})\tanh(\frac{\pi W_{se}}{2\tau})]^{-1}, \quad (19)$$

In the above equations, g is the physical air-gap, d is the secondary aluminum sheet thickness, s the motor slip, G goodness factor of the motor, δ_i the depth of the field penetration in the secondary back-iron, and μ_i is the secondary back-iron permeability which should be calculated using iterative algorithm [22].

For the calculation of the secondary resistance, the conductivity of the secondary sheet should be modified. The effective conductivity of the secondary sheet, σ_e is given by [20]:

$$\sigma_e = \sigma / k_{sk}, \tag{20}$$

in which

$$k_{sk} = \frac{2d}{\delta_s}[\frac{\sinh(2d/\delta_s)+\sin(2d/\delta_s)}{\cosh(2d/\delta_s)-\cos(2d/\delta_s)}], \tag{21}$$

where δ_s is the depth of the field penetration in the secondary sheet which can be calculated by:

$$\delta_s = [\frac{1}{2}(\frac{\pi}{\tau})^2 + \mu_0 \pi f_1 s \sigma]^{-1/2}, \tag{22}$$

In the above equation, f_1 is the primary supply frequency, τ the motor pole pitch, σ is the conductivity of the secondary sheet which is reduced by the factor k_{sk} because of the skin effect. Besides the skin effect, the edge effect reduces the secondary conductivity by the factor k_{tr}. If the latter factor and contribution of the secondary back-iron in conduction of the secondary current are taken into account, the effective conductivity is modified to:

$$\sigma_{ei} = \frac{\sigma}{k_{sk} k_{tr}} + \frac{\sigma_i \delta_i}{k_{tri} d}. \tag{23}$$

The primary referred secondary resistance is defined as [23]:

$$R_2' = X_m / G_e, \tag{24}$$

where G_e is the modified goodness factor of the motor which is given by [20]:

$$G_e = 2\mu_0 f_1 \tau^2 \sigma_{ei} d / (\pi g_e). \tag{25}$$

In secondary sheet linear induction motors, the secondary reactance can be neglected [24]; so, $X_2' \approx 0$. Also, due to low value of the flux density in the air-gap, the core loss is negligible; so, $R_c \approx 0$. In Fig. 1, Q is normalized motor length. The value of Q is obtained by the following equation [9]:

$$Q = L_s R_2' / [(L_m + L_2')V_r], \tag{26}$$

In which, L_s is the primary length, V_r the motor speed, L_m the magnetizing inductance, and L_2' is the secondary leakage inductance which is zero for secondary sheet motors.

Air-gap flux density is given by [20]:

$$B_g = \mu_0 J_m \tau / [\pi g_e \sqrt{1+(sG_e)^2}], \tag{27}$$

where, J_m is the amplitude of the equivalent current sheet which is calculated as follows [20], [25]:

$$J_m = 3\sqrt{2} k_w N I_1 / (\pi \tau). \tag{28}$$

Using (27), the tooth flux density is obtained as:

$$B_t = B_g \tau_s / w_t. \tag{29}$$

Referring to Fig. 1 and doing some mathematical calculations, the following equations for efficiency, power factor, output thrust and normal force are derived:

$$\eta = \frac{F_x 2\tau f_1 (1-s) + 3(s-1) R_m {I_m}^2}{F_x 2\tau f_1 + 3{I_1}^2 R_1}, \tag{30}$$

$$\cos\varphi = [F_x 2\tau f_1 + 3{I_1}^2 R_1] / (3 I_1 V_1), \tag{31}$$

$$F_{xo} = \frac{3{I_1}^2 R_2'}{s 2\tau f_1}[\frac{{R_m}^2 + {X_{m1}}^2}{(R_2'/s + R_m)^2 + {X_{m1}}^2}], \tag{32}$$

$$F_y = \frac{\mu_0 L_s W_s}{4} \frac{1-(\sigma_{ei} d \mu_0 s V_s)^2}{\sinh^2(\pi g_{ei}/\tau) + (\sigma_{ei} d \mu_0 s V_s)^2 \cosh^2(\pi g_{ei}/\tau)} {J_m}^2, \tag{33}$$

In the above equations, R_m is the magnetizing branch resistance in Duncan model which represents the power loss due to end effect and X_{m1} is the modified magnetizing reactance considering end effect which are calculated by the following equations:

$$R_m = R_2'[1-e^{-Q}]/Q, \tag{34}$$

$$X_{m1} = X_m(1-[1-e^{-Q}]/Q), \tag{35}$$

III. SECONDARY BACK IRON SATURATION EFFECTS

The secondary back-iron plays important role in performance of the SLIM. On the one hand, it is used as magnetic flux pass produced by the primary; on the other hand, it is a mechanical support for the secondary of the motor. For proper working of the SLIM, the magnetic field produced by the primary should penetrate in the secondary aluminum sheet as well as the secondary back-iron. Because of the low value of the relative

permeability of the secondary conductor sheet, the field can easily penetrate in whole of it. However, the depth of the field penetration in the secondary back-iron is limited. The field can only penetrate in a limited thickness of the iron. Hence, the whole thickness of the secondary back-iron is not used as magnetic flux pass. Thus, at some operating conditions, due to high value of the flux density, saturation occurs in the back-iron and should be taken in to account in calculations. The saturation factor is given in (17) where the iron relative permeability μ_i should be determined. To do this, an iterative algorithm is employed. First, a proper value for the relative permeability μ_i is assigned. Then, the saturation factor and the depth of the field penetration are calculated using (17) and (18). Then, air-gap leakage factor k_l, Carter's coefficient k_c, magnetizing reactance factor due to edge effect k_{tm} are calculated using (7), (8), and (10). Then, the effective air-gap length and the secondary modified effective conductivity are calculated using (5) and (23). The air-gap flux density is calculated using (27). If the distribution of the flux density through the back-iron takes exponential form, in depth x from the surface of the back-iron, we have:

$$B_i = B_{is} e^{-\frac{x}{\delta_i}} \tag{36}$$

where B_{is} is the flux density on the secondary back-iron surface. By having air-gap flux density, B_{is} is calculated using the following equation:

$$B_{is} = B_g \frac{\tau}{\pi \delta_i} \tag{37}$$

With the obtained flux density, and using the back-iron $B-H$ curve, the relative permeability of the back-iron is calculated. Now, the relative permeability used in the previous calculation step is replaced by the calculated one. With the new obtained relative permeability, the calculations are repeated to obtain a desired convergence.

IV. PERFORMANCE ANALYSIS AND DISCUSION

In this section, the effect of the input frequency on the performance of the SLIM is investigated. The specifications of the SLIM are shown in Table 1. As mentioned in the previous sections, the frequency influences the depth of the field penetration and saturation level of the secondary back-iron. In Fig. 2, the depth of the field penetration in back-iron, its relative permeability, the input impedance and the input current of the SLIM are illustrated. It is seen in this figure that by increasing the frequency, the depth of the field penetration is decreased while the relative permeability of the secondary back-iron is increased. At first, it seemed that by decreasing the depth of penetration, the relative permeability would decrease because of increasing the flux density in limited thickness of the iron. However, the increment in the relative permeability is because of the increasing the input impedance and accordingly decreasing the input current and the air-gap flux density, as the frequency increased. In order to approximately maintain the input current and the air-gap flux density constant, the input voltage is increased by increasing the frequency. So, *V/f* is kept constant. In this case, the results for the same characteristics depicted in Fig. 2 are illustrated in Fig. 3. As expected, it is seen that by increasing the input frequency, the relative permeability of the back-iron decreases. The relative permeability in these figures is obtained by iterative algorithm discussed in the previous section. The magnetizing curve for the sample iron used as back-iron is illustrated in Fig. 4 which has been extracted by experiment. Figure 5 shows outputs of the SLIM versus input frequency. It is seen that increasing the frequency, on the one hand, increases the efficiency; on the other hand, decreases the power factor, the output thrust and the normal force. As the input impedance increases by increasing the frequency, the input current and accordingly the air-gap flux density decreases and causes the output thrust and also the normal force to decrease. As seen in the figure, the normal force becomes negative for the frequencies higher than 262Hz. It means that in mentioned frequency ranges, the repulsive normal force is larger than the attractive one. This phenomenon is because of the reaction of the secondary conductor sheet. For further clarity, the attractive and repulsive normal forces are separately shown in Fig. 6. As it is seen in this figure, although the absolute values of both of the attractive and repulsive normal force decrease by increasing the frequency, the absolute value of the repulsive force is larger than that of attractive one in high frequency ranges. Figure 7 illustrates the depth of

the field penetration and relative permeability of the secondary back-iron versus frequency in different back-iron resistivities. The figure shows that by increasing the back-iron resistivity, the depth of the field penetration is increased as expected from (18). Also, increasing the resisitivity of the back-iron increases the permeability of the iron, and accordingly decreases its reluctance. In Fig. 8, the relative permeability of the back-iron versus the motor speed is illustrated for constant input frequency. As seen in this figure, in low speeds, the frequency in the secondary circuit of the SLIM is high; hence, the value of the relative permeability is low. As the speed increases the relative permeability also increases. It should be noted that in this case, only the frequency of the secondary circuit changes; so, the input impedance of the motor does not change too much to decrease the input current and the air-gap flux density. This is the reason for different behavior of the relative permeability in Figs. 2 and 8.

Table 1: The SLIM specifications

Specification	Values
Phase input voltage, V	220
Primary current density, A/mm^2	6
Primary width, mm	130
Secondary sheet thickness, mm	2.0
Air gap length, mm	5.1
Slip	0.5
Number of pole pairs	2
Number of slots/pole/phase	3
Number of turns/phase	72
Motor length(L_s), m	0.4138
Tooth width, mm	2.9
Slot width, mm	6.8
Slot depth, mm	39.3
Primary weight, Kg	29.34

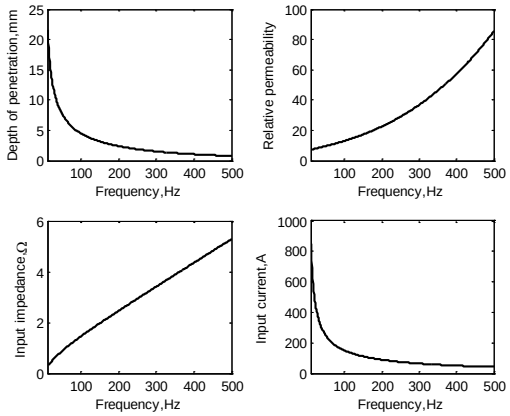

Fig. 2. Frequency effects on different parameters of the SLIM.

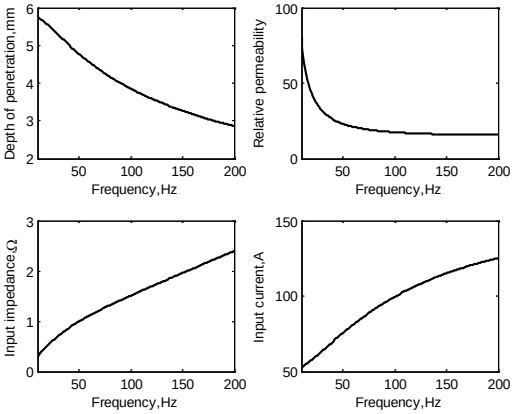

Fig. 3. Frequency effects on different parameters of the SLIM (*V/f* constant).

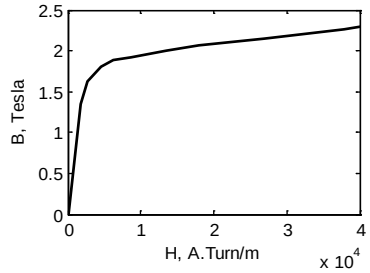

Fig. 4. Back-iron magnetizing curve extracted by experiment.

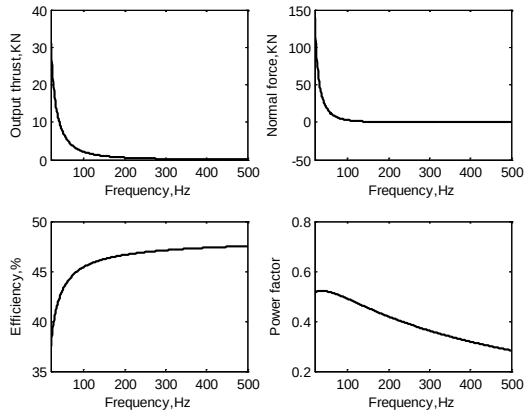

Fig. 5. Frequency effects on different outputs of the SLIM.

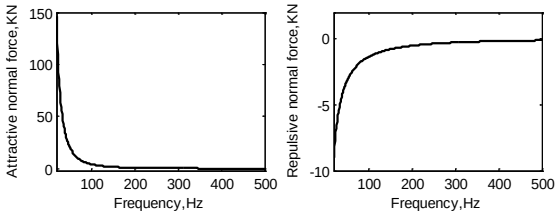

Fig. 6. Frequency effects on attractive and repulsive normal force.

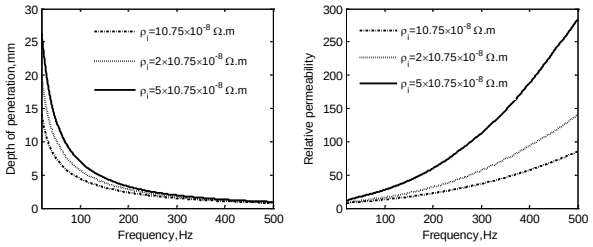

Fig. 7. Frequency effects on different parameters of the SLIM.

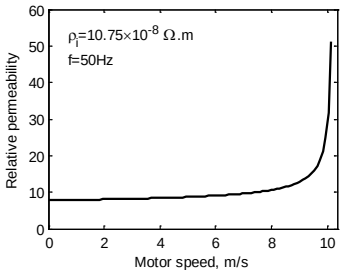

Fig. 8. Relative permeability of the back-iron versus motor speed.

V. FINITE ELEMENT ANALYSIS

In this section, 2-D time-stepping finite element method (FEM) is employed to confirm the analytical results. The SLIM given in Table 1 is used in FEM simulations. In Fig. 9, the flux paths in the different parts of the SLIM is illustrated. The input frequency of the motor is 20Hz. In order to investigate the effect of the frequency on the depth of the field penetration and the secondary back-iron, the simulations are done with input frequency of 20 and 200Hz in constant input current. With input current being constant, only the effects of the input frequency changes are investigated. Figure 10 shows the flux density distribution results for f=20Hz, while in Fig. 11, the flux density distribution results for f=200Hz are illustrated. The magnetizing curve shown in Fig. 4 is used for the back-iron. As seen in Figs. 10 and 11, by increasing the input frequency, the depth of the field penetration is reduced and the flux can only penetrate into a limited thickness of the secondary back-iron. Also, the flux density is increased in those regions. Figure 12 illustrates the distribution of the current density on the secondary back-iron, when the input frequency is 200 Hz. It is also clear in this figure that the depth of the field penetration is limited to a narrow path in the secondary back-iron. The current density in these areas is in the order of $10^7 A/m^2$. This high value of current density produces large local MMFs and causes the flux density to increase and locally saturates the secondary back-iron. To compare the analytical results with the results of the FEM, the simulations have been done in different input frequencies. The efficiency, the power factor, the normal force, and the output thrust are calculated using the FEM. The analytical calculation results are compared with FEM results in Table 2. It is seen in Table 2 that by increasing the input frequency, the efficiency increases while the power factor, the normal force, and the output thrust decrease. These behaviors have been previously deduced from Fig. 5. It can be also seen that the results of the two methods are close enough to each other confirming the analytical calculations.

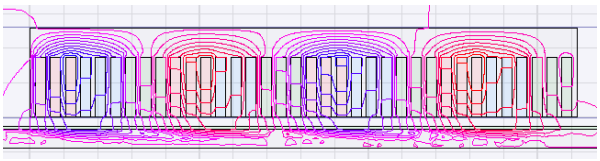

Fig. 9. Flux paths in the moving SLIM ($f = 20Hz$).

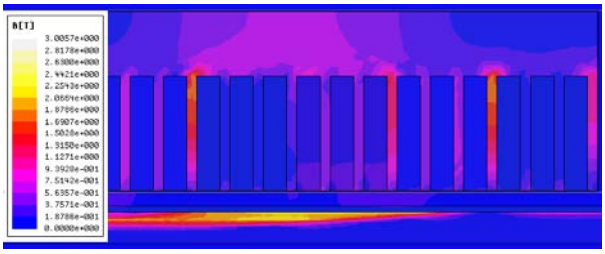

Fig. 10. Flux density distribution in different parts of SLIM ($f = 20Hz$).

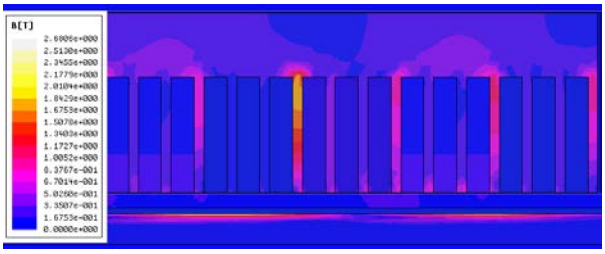

Fig. 11. Flux density distribution in different parts of SLIM ($f = 200Hz$).

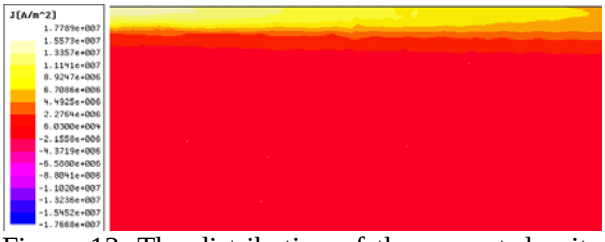

Figure 12. The distribution of the current density on the secondary back-iron ($f = 200Hz$).

VI. CONCLUSION

The magnetic characteristic of the secondary back-iron in the SLIM is affected by the level of the saturation and accordingly the input frequency. So, the performance of the motor mainly depends on the latter. In this paper, the effects of the input frequency on the SLIM outputs are investigated. Analytical equations for the efficiency, the power factor, the normal force and the output thrust of the SLIM are derived considering the longitudinal end effect, iron saturation, transverse edge effect, and skin effect. The results show that increasing the frequency, decreases the active and usable thickness of the secondary back-iron. So, in high frequencies, the thickness of the secondary back-iron can be limited to the depth of the field penetration in the iron. It should be mentioned that besides the magnetic capabilities, the secondary back-iron is used as mechanical support for the secondary sheet which should be taken in to account in design. 2D finite element method is used to confirm the analytical investigations. The FEM results, in which all phenomena are taken into account, are in good agreement with the analytical results. This confirms the validity of the proposed analytical equations and analysis.

Table 2: The calculation and FEM results

		Efficiency, %	Power factor
f=20Hz	Analytical	37.59	0.5252
	FEM	35.71	0.5447
f=50Hz	Analytical	43.20	0.5211
	FEM	41.42	0.5409
f=100Hz	Analytical	45.38	0.4898
	FEM	44.04	0.5093
f=500Hz	Analytical	47.52	0.2824
	FEM	45.97	0.3101
		Normal force, KN	Output thrust, KN
f=20Hz	Analytical	137.18	32.01
	FEM	136.21	32.05
f=50Hz	Analytical	17.91	7.32
	FEM	18.01	7.35
f=100Hz	Analytical	2.89	2.18
	FEM	2.81	2.20
f=500Hz	Analytical	-0.069	0.073
	FEM	-0.060	0.069

REFERENCES

[1] S. Nonaka and T. Higuchi, “Elements of Linear Induction Motor Design for Urban Transit”, *IEEE Trans. Magn.*, vol. 23, no. 5, pp. 3002-3004 , 1989.

[2] S. Yoon, J. Hur, and D. Hyun, “A Method of Optimal Design of Single-Sided Linear Induction Motor for Transit”, *IEEE Trans. Magn.*, vol. 33, no. 5, pp. 4215-4217, 1997.

[3] S. Osawa, M. Wada, M. Karita, D. Ebihara, and T. Yokoi, “Light-Weight Type Linear Induction Motor and Its Characteristics”, *IEEE Trans. Magn.*, vol. 28, no. 4, pp. 3003-3005, 1992.

[4] M. Kitamura, N. Hino, H. Nihei, and M. Ito, “A Direct Search Shape Optimization Based on Complex Expressions of 2-Dimentional Magnetic Fields and Forces”, *IEEE Trans. Magn.*, vol. 34, no. 5, pp. 2845-2848, 1998.

[5] A. H. Isfahani, H. Lesani, and B. M. Ebrahimi, “Design Optimization of Linear Induction Motor

for Improved Efficiency and Power Factor", *IEEE Int. Conf. on Electric Machines Drives, IEMDC*, pp. 988-991, 2007.

[6] A. H. Isfahani, B. M. Ebrahimi, and H. Lesani, "Design Optimization of a Low-Speed Single-Sided Linear Induction Motor for Improved Efficiency and Power Factor", *IEEE Trans. Magn.*, vol. 44, no. 2, pp. 266-272, 2008.

[7] C. Lucas, Z. Nasiri, G. and F. Tootoonchian, "Application of an Imperialist Competitive Algorithm to Design of Linear Induction Motor", *Energy Conversion and Management*, vol. 51, pp. 1407-1411, 2010.

[8] D. H. Im, S. C. Park, and J. W. Im, "Design of Single-Sided Linear Induction Motor using the Finite Element Method and SUMT", *IEEE Trans. Magn.*, vol. 29, no. 2, pp. 1762-1766, 1993.

[9] J. Duncan, "Linear Induction Motor-Equivalent Circuit Model", *IEE Proc. Electric Power Appl.*, vol. 130, no. 1, pp. 51-57, 1983.

[10] W. Xu, J. G. Zhu, Y. Zhang, Y. Li, Y. Wang, and Y. Guo, "An Improved Equivalent Circuit Model of a Single-Sided Linear Induction Motor", *IEEE Trans. Vehicular Tech.*, vol. 59, no. 5, pp. 2277-2289, 2010.

[11] W. Xu, J. G. Zhu, Y. Zhang, Z. Li, Y. Li, Y. Wang, Y. Guo, and W. Li, "Equivalent Circuits For Single-Sided Linear Induction Motors", *IEEE Trans. Ind. Appl.*, vol. 46, no. 6, pp. 2410-2423, 2010.

[12] S. G. Lee, H. Lee, S. Ham, C. Jin, H. Park, and J. Lee, "Influence of the Construction of Secondary Reaction Plate on the Transverse Edge Effect in Linear Induction Motor", *IEEE Trans. Magn.*, vol. 45, no. 6, pp. 2815-2818, 2009.

[13] A. Z. Bazghaleh, M. R. Naghashan, and M. R. Meshkatoddini, "Optimum Design of Single-Sided Linear Induction Motors for Improved Motor Performance", *IEEE Trans. Magn.*, vol. 46, no. 11, pp. 3939–3947, 2010.

[14] A. Z. Bazghaleh, M. R. Naghashan, M. R. Meshkatoddini, and H. Mahmoudimanesh, "Optimum Design of High Speed Single-Sided Linear Induction Motor to Obtain Best Performance", *IEEE Conf. Power Electronics & Electrical Drive, Automation & Motion, SPEEDAM*, pp. 1222-1226, 2010.

[15] A. Z. Bazghaleh, M. R. Naghashan, M. R. Meshkatoddini, and H. Mahmoudimanesh, "Optimum Design of High Speed Single-Sided Linear Induction Motor using Particle Swarm Optimization", *IEEE Conf. Power Electronics & Drive Systems & Technologies, PEDSTC*, pp. 329-334, 2010.

[16] J. F. Gieras, G. E. Dawson, A. R. Easthan, "A New Longitudinal End Effect Factor for Linear Induction Motor", *IEEE Trans. Energy Convers.*, vol. 2, no. 1, pp. 152-159, 1987.

[17] R. C. Creppe, J. A. C. Ulson and J. F. Rodrigues, "Influence of Design Parameters on Linear Induction Motor End Effect", *IEEE Trans. Energy Convers.*, vol. 23, no. 2, pp. 358-362, 2008.

[18] J. Lu and W. Ma., "Research on End Effect of Linear Induction Machine For High-Speed Industrial Transportation", *IEEE Trans. Plasma Sci.*, vol. 39, no. 1, pp. 116-120, 2011.

[19] T. Yang, L. Zhou, and L. Li, "Influence of Design Parameters on end Effect in Long Primary Double-Sided Linear Induction Motor", *IEEE Trans Plasma Sci.*, vol. 39, no. 1, pp. 192-197, 2011.

[20] I. Boldea and S. A. Nasar, *Linear motion electromagnetic devices*, Taylor & Francis, New York, 2001.

[21] S. A. Nasar and I. Boldea, Linear electric motors, Prentice-Hall, New Jersey, 1987.

[22] M. Mirsalim, A. Doroudi, and J. S. Moghani, "Obtaining the Operating Characteristics of Linear Induction Motors: A New Approach", *IEEE Trans. Magn.*, vol. 38, no. 2, pp. 1365-1370, 2002.

[23] E. R. Laithwaite, Induction machines for special purposes, George Newnes Limited, London 1996.

[24] R. M. Pai, I. Boldea, and S. A. Nasar, "A Complete Equivalent Circuit of a Linear Induction Motor with Sheet Secondary", *IEEE Trans. Magn.*, vol. 24, no. 1, 1988.

[25] J. F. Gieras, *Linear Induction Drives*, Oxford University Press, New York, 1994.

Abbas Shiri was born in Hashtrood, Iran in 1980. He received the B.Sc. degree from Tabriz University and M.Sc. degree from Iran University of Science and Technology (IUST) both in electrical engineering in 2004 and 2006, respectively. He is currently working toward Ph.D. degree in electrical engineering at IUST.

His areas of research interests include linear electric machines, electromagnetic systems and actuators, electrical machine design and modeling.

Abbas Shoulaie was born in Isfahan, Iran, in 1949. He received the B.Sc. degree from Iran University of Science and Technology (IUST), Tehran, Iran, in 1973, and the M.Sc. and Ph.D. degrees in electrical engineering from U.S.T.L, Montpellier, France, in 1981 and 1984, respectively.

He is a Professor at the department of Electrical Engineering, IUST. He is the author of more than 100 journal and conference papers in the field of power electronics, electromagnetic systems, electrical machine, linear machine and HVDC.